Radio Science

RESEARCH ARTICLE
10.1029/2020RS007220

Drift Velocity Estimation of Ionospheric Bubbles Using GNSS Observations

Ana L. C. Souza[1], Paulo O. Camargo[1], Marcio T. A. H. Muella[2], and Flavia Tardelli-Coelho[2]

[1]Departament of Cartography, Universidade Estadual Paulista-UNESP, Presidente Prudente, São Paulo, Brazil, [2]Universidade do Vale do Paraíba-UNIVAP, Instituto de Pesquisa e Desenvolvimento, Laboratório de Física e Astronomia, São José dos Campos, São Paulo, Brazil

Key Points:

- Global navigation satellite systems observations to infer plasma bubbles velocities
- Airglow images to confirm the plasma bubbles velocities

Correspondence to:
A. L. C. Souza,
ana.lucia@unesp.br

Citation:
Souza, A. L. C., Camargo, P. O., Muella, M. T. A. H., & Tardelli-Coelho, F. (2021). Drift velocity estimation of ionospheric bubbles using GNSS observations. *Radio Science*, *56*, e2020RS007220. https://doi.org/10.1029/2020RS007220

Received 15 OCT 2020
Accepted 6 JUL 2021

Abstract Equatorial plasma bubble (EPB) irregularities are large-scale plasma depleted structures that exist in the equatorial and low-latitude ionosphere. Thus, particularly in these regions, much attention must be given to the effects of the EPBs in the life critical applications based on global navigation satellite systems (GNSS). The study on the dynamics of plasma bubbles, particularly in the determination of their drift velocities, and their impact on ground-based augmentation system is of fundamental importance for civilian aviation. In this regard, we proposed a methodology to estimate the zonal drift velocities of the plasma bubble irregularities using slant total electron content (TEC) measurements derived from two spaced ground-based GNSS receivers. The experiments were performed with the purpose to evaluate if the drift velocities obtained using the methodology proposed in this study agree with the velocities deduced from all-sky imaging systems. The results revealed that the TEC-estimated mean eastward drift velocities were comparable with the values deduced from the airglow techniques, and with the results obtained from previous studies. Therefore, the methodology proposed in this work to infer the plasma bubble drift velocities seem to have the potential in future investigations to provide a new data source in this field.

1. Introduction

The Earth's atmosphere is known to have great influence on the propagation of radio wave signals from Global Navigation Satellite Systems (GNSS). The ionospheric layer, which comprises the partially ionized portion of the Earth's atmosphere between about 60–1,000 km height, contains an appreciably dense plasma capable of modifying the amplitude, phase and polarization of GNSS signals. Moreover, the presence of inhomogeneities in the electron density distribution of the ionospheric plasma can also provoke severe amplitude and phase fluctuations of a satellite power signal received on the ground. Such inhomogeneities in the ionosphere are called plasma bubble irregularities. These bubbles are in fact plasma-depleted density irregularity structures developed in the equatorial ionosphere shortly after sunset. There is a consensus in the literature that the primary mechanism responsible for the generation of the equatorial plasma bubble (EPB) irregularities is the gravitational Rayleigh–Taylor plasma instability (Abdu, 2005; Haase et al., 2010; Ji et al., 2011; Kelley, 2009; Mendillo et al., 2005).

As the EPBs rise and grow up vertically through the ionospheric F region, they also tend to expand along the geomagnetic field lines to off-equatorial latitudes and to drift eastward in the zonal direction (Kelley, 2009; Sahai et al., 2000). Thus, particularly at equatorial and low-latitudes regions, much attention must be given to the effects of the EPBs on current positioning/navigation applications based on GNSS (Bumrungkit et al., 2018; Rungraengwajiake et al., 2015), including the satellite-based augmentation systems and ground-based augmentation systems (GBAS). For example, there is a concern for life critical GNSS navigation, as on the air transportation of passengers, where the system performance, integrity and reliability under all conditions is of great importance (Saito et al., 2017). Basically, the GBAS is used near an airport to augment the existing GNSS satellites by providing positioning improvement to aircraft approach and landing. Recently, the impact of ionospheric plasma bubble irregularities on GBAS have been investigated by several researchers (e.g., Fujiwara & Tsujii, 2016; Saito et al., 2017; Srinivas et al., 2014; Yoon et al., 2019).

The Global Positioning System (GPS), the principal component of the current GNSS, was declared fully operational in 1995. Since then, the activity and the spatial-temporal variability of EPBs have been investigated

by many researchers using GNSS receivers operating concurrently with other different instruments and techniques (e.g., Prol, Hernández-Pajares, et al., 2018; Silva et al., 2019; Sobral et al., 2009; Wang et al., 2015; Yang & Liu, 2018). For example, in the work of Sobral et al. (2009), the zonal dynamics of the large-scale plasma bubbles inferred from OI 630.0 nm airglow all-sky images were compared with simultaneous measurements of GPS-estimated irregularity zonal drifts. The authors showed that the smaller-scale irregularities detected by the GPS scintillation monitors always drifted with velocities larger than the airglow zonal velocities. They argued that such differences are due to the presence of a positive velocity gradient (shear) between the altitudes of the airglow emitting layer (~250 km) and of the GPS scintillations, where the probed irregularities are located around F-peak heights (~350 km). Wang et al. (2015) showed that the morphology and temporal variability of ionospheric plasma bubbles can be studied from concurrent observations of digital ionosonde, GPS and in situ ion density measurements. Prol, Hernández-Pajares, et al. (2018) used GNSS tomographic technique, OI 630.0 nm airglow all-sky images and radio occultation (RO) measurements to investigate the vertical and horizontal distributions of ionospheric plasma bubbles. Yang and Liu (2018) also analyzed RO measurements to study the day-to-day variability of ionospheric F-region irregularities by comparing with simultaneous GNSS scintillation and total electron content (TEC) measurements. Silva et al. (2019) analyzed TEC depletions associated to EPBs in order to estimate their zonal drift velocities between two GNSS receiving stations located in the Brazilian sector. The authors compared the TEC-estimated irregularity drifts with those obtained simultaneously from all-sky optical instruments and reported comparable magnitudes of zonal velocities. It is worthwhile mentioning that recently, the estimations of the irregularity zonal drift velocities have increased in importance with the aim to mitigate the ionospheric space weather effects on current positioning and navigation technologies (e.g., Muella et al., 2017 and references cited therein).

It was noticed from the studies mentioned above that the GNSS and airglow techniques are commonly used to investigate the temporal evolution and spatial development of the EPBs. The airglow all-sky imagers monitor the plasma bubbles in a region of ~15° in latitude and longitude and have the advantage to provide two-dimensional horizontal images with good resolution. However, the airglow imagers depend on weather conditions, where clouds and precipitation can disrupt the plasma bubbles imaging, or even can suffer interference due to moonlight brightness. Otherwise, the observations of EPBs from GNSS reference networks are not dependent on weather conditions and have also the advantage to provide high spatial and temporal resolution in a wide area of coverage. Despite the limitations of the optical technique, simultaneous analysis of airglow and GNSS measurements has been presented as a useful tool to investigate the dynamical and spatial structures of the EPBs. In this regard, we propose in this study a methodology to infer the zonal drift velocities of the ionospheric plasma bubble irregularities using slant TEC measurements derived from two close ground-based GNSS receivers. Since the drift velocities of ionospheric irregularities is an important parameter to the assessment of the GBAS performance in the civilian air aviation, the GNSS stations used in this work to estimate the zonal drifts are located near the International Airport of Rio de Janeiro (RJ), Brazil. In addition, case studies of zonal velocities derived from TEC measurements are compared with estimations from airglow technique.

2. Zonal Drift Velocity Estimation Based on GNSS Slant TEC Measurements

It is well known that the EPB irregularities formed during sunset hours are field-aligned structures which tend to propagate eastward toward the nocturnal ionosphere. As the EPBs move eastward, it is possible to estimate their zonal velocities by capturing depletions at slant TEC level from two stations located in the east-west direction.

In this context, the EPB zonal drift velocity (in $m.s^{-1}$) can be obtained as follows:

$$V = \frac{D_{k1-k2}}{t_{k1-k2}} \quad (1)$$

where D_{k1-k2} represents the longitude distance (in meters) between two GNSS reference stations and t_{k1-k2} (in seconds) denotes the time that the EPB travels from one station to the other station. Thus, we estimate the plasma bubble drifts from the depletion pattern of slant TEC observations. The traveling time of plasma bubbles moving between the stations is estimated from the time lag of slant TEC pattern calculated

using autocorrelation and cross-correlation techniques. The autocorrelation $\left(R_{R1/R1}\right)$ and cross-correlation $\left(R_{R1/R2}\right)$ functions between two signals with slant TEC time series are given by (Bumrungkit et al., 2014):

$$R_{R1/R1} = \frac{\sum_{i=1}^{n}\left(\mathrm{TEC}_{R1_i} - \overline{\mathrm{TEC}_{R1}}\right)\left(\mathrm{TEC}_{R1_{i+1}} - \overline{\mathrm{TEC}_{R1}}\right)}{\sqrt{\sum_{i=1}^{n}\left(\mathrm{TEC}_{R1_i} - \overline{\mathrm{TEC}_{R1}}\right)^2 \sum_{i=1}^{n}\left(\mathrm{TEC}_{R1_{i+1}} - \overline{\mathrm{TEC}_{R1}}\right)^2}}, \tag{2}$$

$$R_{R1/R2} = \frac{\sum_{i=1}^{n}\left(\mathrm{TEC}_{R1_i} - \overline{\mathrm{TEC}_{R1}}\right)\left(\mathrm{TEC}_{R2_i} - \overline{\mathrm{TEC}_{R2}}\right)}{\sqrt{\sum_{i=1}^{n}\left(\mathrm{TEC}_{R1_i} - \overline{\mathrm{TEC}_{R1}}\right)^2 \sum_{i=1}^{n}\left(\mathrm{TEC}_{R2_i} - \overline{\mathrm{TEC}_{R2}}\right)^2}}, \tag{3}$$

where TEC_{R1_i} and TEC_{R2_i} are the slant TEC values for the two reference stations ($R1$ and $R2$) into the signal time series, and $\overline{\mathrm{TEC}_{R1}}$ and $\overline{\mathrm{TEC}_{R2}}$ represent the mean values of slant TEC, i represents time period that the TEC data is estimated equal to 15 s.

In this work, the slant TEC has been derived from the pseudorange (TEC_P) and carrier phase (TEC_L) measurements and can be expressed as follows:

$$\mathrm{TEC}_P = K\left(P_2 - P_1\right), \tag{4}$$

$$\mathrm{TEC}_L = K\left(L_1 - L_2\right), \tag{5}$$

where P_1, P_2 and L_1, L_2 are pseudorange and carrier phase measurements at F1 (1,575.42 MHz) and F2 (1,227.60 MHz) of GPS L-band frequencies, respectively, and the constant $K = 9.52$ (m^{-1} TECU). The slant TEC is expressed in Total Electron Content Unit (TECU), where 1 TECU represents 1×10^{16} electrons/m^2.

The TEC measured by pseudorange is noisier than obtained by the carrier phase; however, the phase has an initial ambiguity. We estimated the ambiguities using the so-called phase leveling, as proposed by Mannucci et al. (1998) and Ciraolo et al. (2007). In this method, which is based on code information, the difference between ambiguity terms is determined by the mean difference of the ionospheric delay calculated using phase and code over one arc of continuous data with no cycle slips (Prol, Camargo, et al., 2018). Thus, the slant TEC is obtained by the expression:

$$\mathrm{TEC}_{Level} = \mathrm{TEC}_L + \left(\overline{\mathrm{TEC}_P - \mathrm{TEC}_L}\right), \tag{6}$$

where $\left(\overline{\mathrm{TEC}_P - \mathrm{TEC}_L}\right)$ represents the mean difference of the TEC values obtained from the pseudorange and carrier phase measurements. Once the leveling ambiguities are corrected, the next step in the TEC estimation is the correction of the differential code biases (DCBs) of the satellites and receivers. This correction can be applied as follows:

$$\mathrm{TEC} = \mathrm{TEC}_{Level} + b_r + b^s, \tag{7}$$

where b_r and b^s are the receiver and satellite DCBs, respectively. The GPS satellite DCBs are obtained from IONosphere map Exchange format files, and the receiver DCBs are calculated by the weighted mean of the difference between the carrier phase measurements and the leveling ambiguity, the satellite DCBs, and the calculated TEC (e.g., Prol, Camargo, et al., 2018). Since TEC in Equation 7 is directly calculated along the path of the GPS signal from each satellite to the receiver, the higher order effects of the ionosphere are neglected and thus, it denotes the slant TEC values. For the zonal drift estimations, the TEC has been calculated from GNSS data using 1/15s sampling rate. For the TEC estimation, it was considered, for all satellites, the elevation angle above 20°. According to Brassarote et al., 2018, this angle mask ensures a good coverage of the local ionosphere over the observation site and was adopted to reduce the effects of low elevation angles, such as multipath and tropospheric effects.

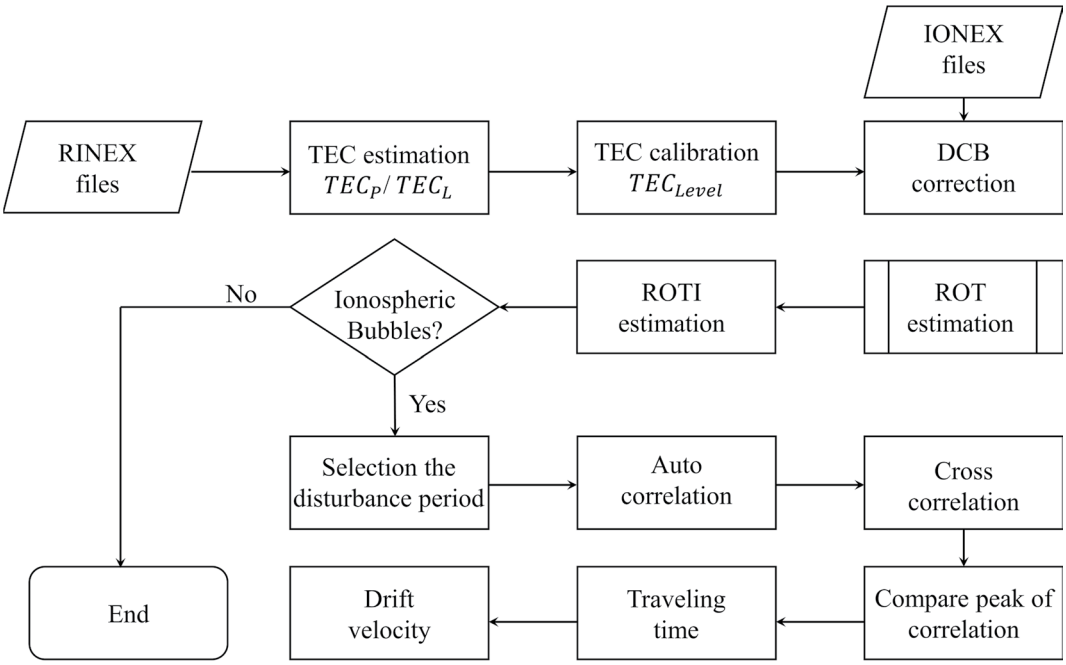

Figure 1. Flowchart of the ionospheric plasma bubble zonal drift velocity estimation based on the Global Positioning System (GPS) total electron content (TEC) measurements.

After the TEC calculation, we estimated the Rate of TEC Index (ROTI) in order to check the strength of the plasma bubble structures being crossed by the GPS signals. This step was adopted to select the most significant events of plasma bubbles which zonal drift velocities would be calculated. The ROTI is obtained here from the standard deviation of the Rate of slant TEC (ROT) over a time interval of 5 min. According to Pi et al. (1997) the ROTI can be calculated as,

$$\mathrm{ROTI} = \sqrt{\left\langle \mathrm{ROT}^2 \right\rangle - \left\langle \mathrm{ROT} \right\rangle^2}, \tag{8}$$

where $< >$ denotes the averaging ROT during N epochs. The ROT is obtained from the difference of slant TEC at two consecutive time epochs; where Δt is the time interval. The unit of ROT is TECU/min. The ROT can be calculated as follows,

$$\mathrm{ROT} = \frac{\mathrm{TEC}_{t_2} - \mathrm{TEC}_{t_1}}{t_2 - t_1} = \frac{\Delta \mathrm{TEC}}{\Delta t}. \tag{9}$$

It is well known that fluctuations larger than 0.5 TECU/min indicate the presence of ionospheric plasma bubble irregularities (Stefanello et al., 2015). Hence this is a criterion used to identify the plasma bubble and to select the time periods for zonal drift estimation. Simultaneously with the observed fluctuation in ROT and the associated increase in the ROTI, the next step is to compare the signatures of slant TEC depletion patterns detected from a same satellite signal at both reference stations. If the difference of slant TEC depletion is larger than 1 TECU at both stations, then the traveling time of plasma bubbles is estimated for zonal drift calculation. The flowchart in Figure 1 presents the steps considered in this work for plasma bubble zonal drift velocity estimation.

Finally, the plasma bubble zonal velocities derived from slant TEC measurements are compared with velocities inferred from all-sky imaging observations of the OI 630 nm nightglow emissions. In this optical technique, the OI 630 nm emission images show intensity depletion bands associated to plasma bubbles. Then, by observing the motion of the depleted structures during successive OI 630 nm emissions, we infer the ionospheric plasma bubble zonal drift velocities. A detailed description of the methodology for ionospheric

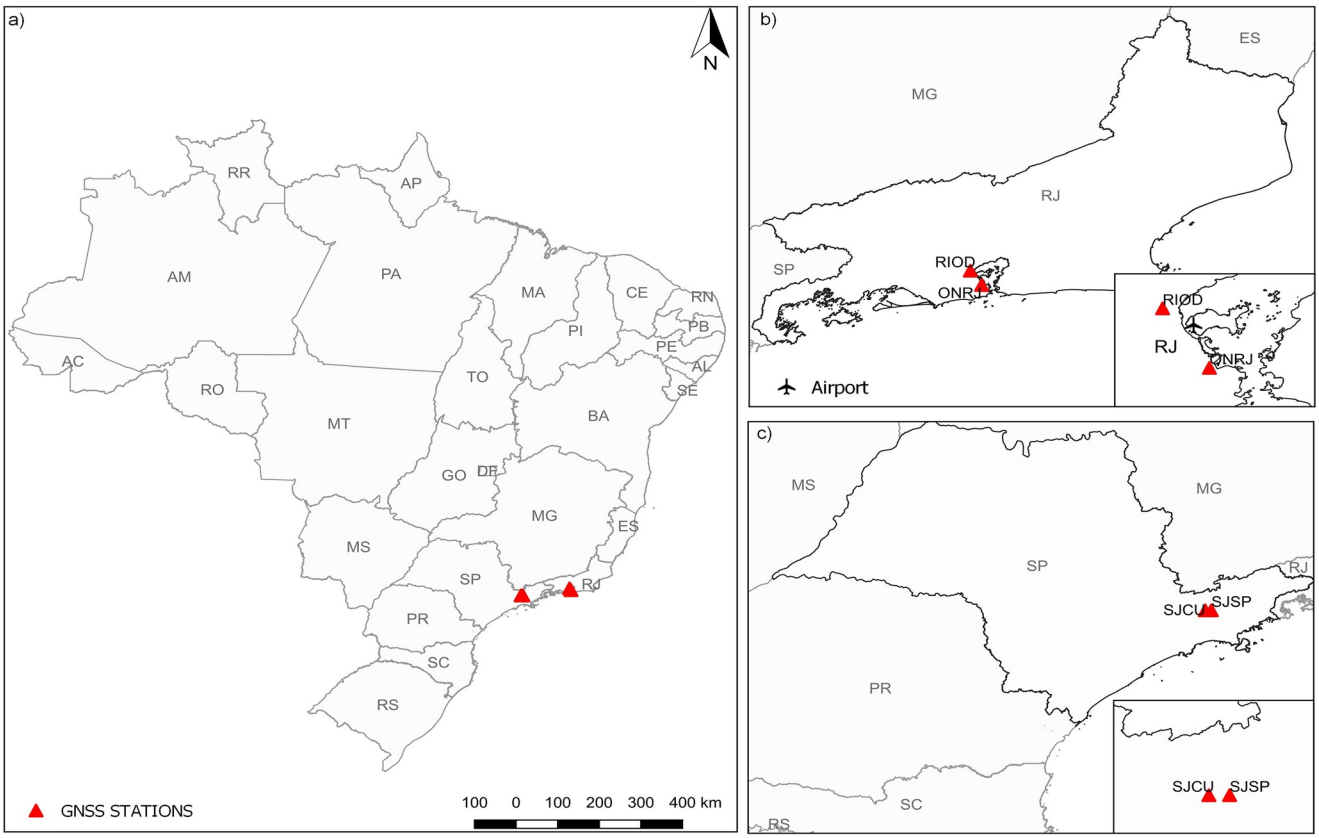

Figure 2. (a) A map showing the localization of the global navigation satellite systems (GNSS) stations in Brazil; (b) The reference stations of RIOD and ONRJ near the Tom Jobim International Airport, in Rio de Janeiro (RJ); (c) The observatories of SJSP and SJCU in São José dos Campos.

zonal drift calculation using OI 630 nm all-sky imaging systems will not be repeated here but can be found in the work of Pimenta et al. (2001) and Abalde et al. (2004).

3. Experimental Setup

In this work we have used GNSS data of four reference stations from Brazilian Network for Continuous Monitoring (RBMC). Two of these stations are located near Tom Jobim International Airport, in RJ, Brazil. One of the observatories in RJ is named RIOD (22.78°S; 43.30°W) and the other is ONRJ (22.81°S; 43.22°W). The longitude distance between the sites of RIOD and ONRJ is ~9,000 m. The other two observatories are named SJSP (23.21°S; 45.86°W) and SJCU (23.21°S; 45.96°W), and both are localized near the international airport of São José dos Campos/São Paulo, Brazil. The longitude distance between these sites is ~10,200 m. The stations of SJSP and SJCU are also part of the CIGALA/CALIBRA (Concept for Ionospheric Scintillation Mitigation for Professional GNSS in Latin America/Countering GNSS high Accuracy applications Limitations due to Ionospheric disturbances in Brazil) network. Figure 2a shows a map with the localization of the GNSS reference stations in the Brazilian territory, and Figures 2b and 2c show the surroundings of the observatories at RJ and São José dos Campos. It is important to note that for these longitude distances (9,000–10,200 m) the irregularity structures do not change significantly during their course. The same plasma bubble structure are seen above the stations, making it possible to identify the same temporal variation of the TEC pattern depletion with high correlation between the signals.

In this study, we present the results of three cases of plasma bubble drifts. The first case to be analyzed here occurred on January 6th, 2014 (DOY 006), and the observations were carried out in the stations of RIOD and ONRJ. The results of the event on DOY 006 will be present in this section for a better illustration of the experimental setup. The other two cases occurred on October 24th, 2014 (DOY 297) and December

17th, 2014 (DOY 351), and the results will be presented in Section 4. The zonal drifts of the plasma bubbles for the events on DOYs 297 and 351 were estimated for the stations of SJSP and SJCU. The results of the drift velocities derived for the observatories of São José dos Campos are compared with the plasma bubble drifts inferred from OI 630.0 nm nightglow emissions. Our observations were limited to night times during 1800–0600 LT. The days for the three cases analyzed in this work were geomagnetically quiet with ΣKp index ≤ 24. The cases occurred during the year of solar maximum of the current solar cycle 24, when the solar index F10.7 attained 197.2, 224.8 and 178.8 *sfu* (*sfu* = 10^{-22} W.m^{-2}.Hz^{-1}) for the DOYs 006, 297 and 351, respectively.

The top panels in Figure 3 show the temporal variation of slant TEC calculated from the signals received by satellites PRN 03 (Figure 3a) and PRN 32 (Figure 3b), and recorded by the GPS receivers installed in the reference stations of ONRJ and RIOD on DOY 006 of 2014. For the satellite PRN 03 the estimated slant TEC at ONRJ (black line) and RIOD (red line) present highly correlated signatures of strong depletions between around 02–05 UT (BST = 7UT–3.0 h). Note that the depletion patterns are very similar, but they appear as a slight time shift between stations of ONRJ and RIOD. These slant TEC depletions indicate that the overhead ionosphere is disturbed by ionospheric plasma bubble irregularities. A maximum TEC depletion of ∼21 TECU was observed between around 03–04 UT for satellite PRN 03. For the satellite PRN 32 it is possible to see that the TEC estimated at both stations passed through short maxima and minima between around 03–04 UT, simultaneous with the strong depletion observed from signals of satellite PRN 03. This reveals that the signals received from both satellites are crossing the same irregularity structure. However, it is also clear noticed that the TEC depletions observed for satellite PRN 32 (maximum of ∼7 TECU) are weaker than those observed for satellite PRN 03. Such differences in the TEC depletions may be attributed to the differences in the sector of the sky where the satellite signals are puncturing the plasma bubble structures.

The panel in Figure 3c show the ROTI calculated for both satellites PRN 03 and PRN 32. The results reveal that from 00 UT to 04 UT the index attained values between about 0.05 and 0.2, which can be classified as moderate levels of changes in TEC caused by EPB irregularities (Pereira and Camargo, 2017). Once TEC depletions and ROTI indicated the presence of plasma bubbles in the ionosphere, the difference in the TEC levels between the reference stations of RIOD and ONRJ was computed. The panels (d and e) in Figure 3 show the TEC differences calculated for satellites PRN 03 and 32, respectively. The difference attained ∼4 TECU at around 02:30 UT for satellite PRN 03 and exceeded 2.5 TECU close to 04 UT for satellite PRN 32. Thus, the time periods between around 00–05 UT when the TEC difference is greater than the threshold of 1 TECU was selected for autocorrelation and cross-correlation analysis.

The time lags of the signals between the two receivers were measured quantitatively using the cross-correlation and autocorrelation techniques. Then from the time lags we estimate the traveling time of plasma bubbles. For example, in Figures 3f and 3g the red lines show the cross-correlation of slant TEC between RIOD and ONRJ stations as obtained from PRN 03 and 32, respectively. Also, in the panels (f and g) of Figure 3 the black lines show the autocorrelation of slant TEC for RIOD reference station as calculated from PRN 03 and 32, respectively. For PRN 03 the maximum autocorrelation occurred at epoch 301 and the maximum cross-correlation occurred at epoch 306, which provides a traveling time of 75 s. In this regard, considering the longitude distance of 9,000 m between the two stations the plasma bubble drift velocity was ∼120 m/s. Whereas for satellite PRN 32 the maximum autocorrelation occurred at epoch 121 and the maximum cross-correlation occurred at epoch 116, also providing a traveling time of plasma bubbles of 75 s and a drift velocity of 120 m/s. We assumed the altitude of the ionospheric irregularity layer to be 350 km above the Earth surface, the same height considered in the TEC estimation

In order to analyze the accuracy of the method, the TEC data were estimated using the 30 s data sampling. Figure 4 shows the correlation and the cross-correlation of slant TEC between RIOD and ONRJ stations as obtained from PRN 03 and 32 using 30 s data sampling. Considering the satellite PRN 03 the maximum autocorrelation occurred at epoch 151 and the maximum cross-correlation occurred at epoch 153, which provides a traveling time of 90 s. In this regard, considering the longitude distance of 9,000 m between the two stations the plasma bubble drift velocity was ∼100 m/s. Whereas for satellite PRN 32 the maximum autocorrelation occurred at epoch 59 and the maximum cross-correlation occurred at epoch 57, also providing a traveling time of plasma bubbles of 60 s and a drift velocity of 150 m/s. This difference can be associated to the rate data sampling.

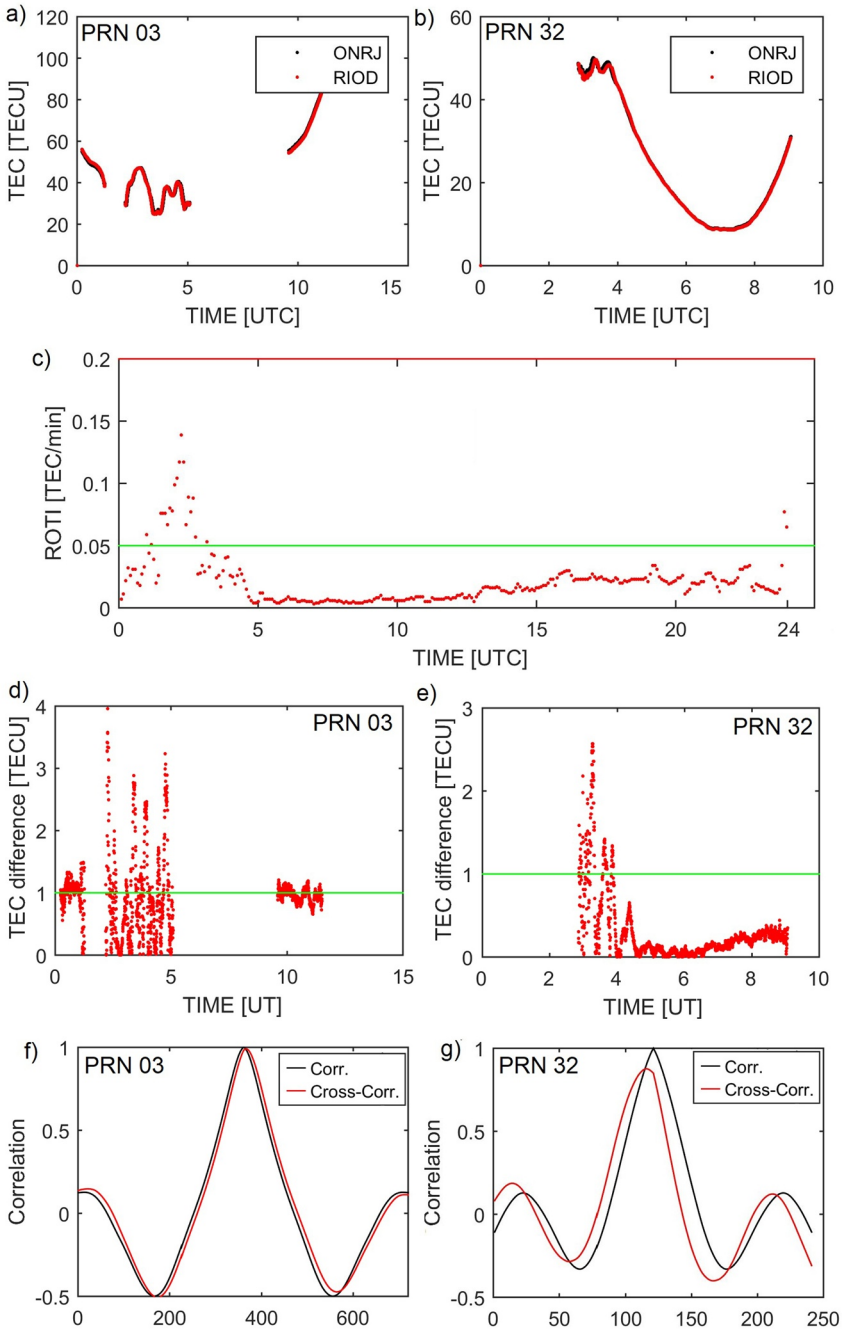

Figure 3. (a) Slant total electron content (TEC) values estimated for Global Positioning System (GPS) satellite PRN 03 on DOY 006 at ONRJ (black line) and RIOD (red line) reference stations; (b) The same as in panel (a) but for GPS satellite PRN 32; (c) ROTI calculated from TEC estimations; (d) Difference in the TEC levels between the reference stations of RIOD and ONRJ as estimated for satellite PRN 03; (e) The same as in panel (a) but for GPS satellite PRN 32; (f) Cross-correlation between RIOD and ONRJ stations (red line) and autocorrelation for RIOD reference station (black line) as obtained from slant TEC estimations of satellite PRN 03 considering 15 s data sampling; (g) The same as in panel (f) but for satellite PRN 32.

Considering the fact that the signals received from satellites PRN 03 and 32 are crossing the same irregularity structure, the velocities should be quite similar. For the 30 s data sampling the velocities show a significant discrepancy of 50 m/s, while the velocities obtained with smallest data sampling were similar for both satellites. Therefore, the results considering 15 s data sampling showed to be more accurate. We

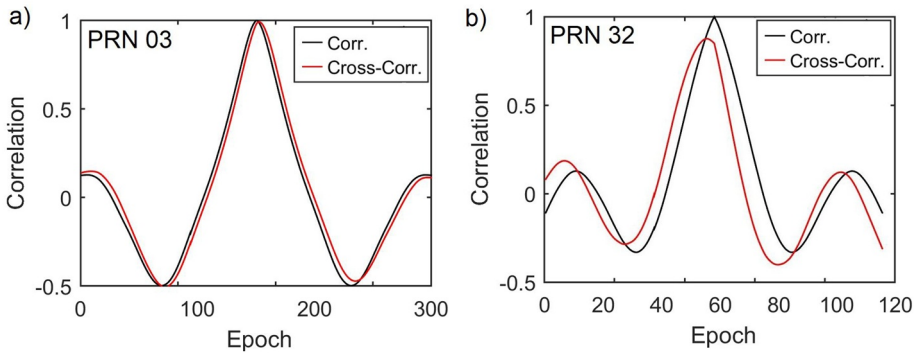

Figure 4. (a) Cross-correlation between RIOD and ONRJ stations (red line) and autocorrelation for RIOD reference station (black line) as obtained from slant total electron content (TEC) estimations of satellite PRN 03, considering 30 s data sampling; (b) The same as in panel (a) but for satellite PRN 32.

can conclude that the smaller the sampling data the better is the accuracy of the proposed method. It is important to note that the smallest sampling data provided by the RBMC network, free access, is equal to 15 s.

4. Results and Discussions

In this Section, we present the results of plasma bubble drift velocities estimated, using the 15 s data sampling, in the observatories of São José dos Campos on October 24th, 2014 (DOY 297) and December 17th, 2014 (DOY 351). Figure 5 presents the results of slant TEC (1st column), autocorrelation and cross-correlation (2nd column), the elevation angles (3rd column), and comparison between the difference TEC and S_4 values (4th column), of the GPS satellites PRN 18, 21, 22, and 25 estimated for the reference stations of SJCU and SJSP on DOY 297. The S_4 data for SJCU reference station were obtained using the ISMR Query Tool (Vani et al., 2017). We considered the scintillation index due to higher S_4 values, which in general is associated with TEC depletions, as can be seen in Figures 5 and 6 (4th column). We can note for all satellites the signatures of TEC depletions associated with plasma bubble irregularities between around 00–05 UT. The depletions in TEC varied from 10 to 35 TECU. We can also note from the TEC plots for satellites PRN 21 and 25 lack of data associated to loss of lock in the channel of the GPS receivers. This loss of lock is usually associated with the presence of ionospheric scintillations. At 4th column in Figure 5, we compared the TEC difference between the reference stations (SJCU and SJSP), that indicates the plasma bubble presence, with the S_4 values. The comparison demonstrated a strong correlation between higher S_4 values and TEC depletion. The highest scintillation values were found when the TEC data were interrupted. This behavior confirms that the loss of receiver lock was caused by the ionospheric scintillation. For example, loss of signal lock occurred between around 02:30–03:30 UT for satellite PRN 21 and the TEC could not be calculated throughout the elapsed time, due to scintillations. The presence of large-scale plasma bubble irregularities are associated with ionospheric scintillation, these total interruptions in the received signals occur when the radio waves cross in the ionosphere a region of very strong phase fluctuations and extremely intense TEC gradients. When strong scintillations occurs enough to cause loss of lock, the TEC cannot be calculated, and consequently, the plasma bubble drift velocities cannot be estimated.

From top to bottom the 2nd column in Figure 5 show, respectively, for satellites PRN 18, 21, 22 and 25 the cross-correlation between SJCU and SJSP stations (red line) and the autocorrelation for SJCU reference station (black line). As described in Sects. Two and three these measures of association between the TEC signals were used to estimate the plasma bubble drift velocities. As also noted from Figure 5, it is important to point out that for all satellites the elevation angle was above 35° (3rd column). It is worthwhile mentioning that for all satellites the strong depletions were associated with large values of TEC above 50 TECU. In general, the TEC values increase as the satellite elevation angle decreases as consequence of the increase in the length of the signal path through the ionosphere. However, for the satellites PRN 18 and 21 the depletions were associated with the decrease in the TEC and with the decrease in the elevation angle. Such decrease in TEC may be related to the natural redistribution of the electron density in the ionosphere that tend to

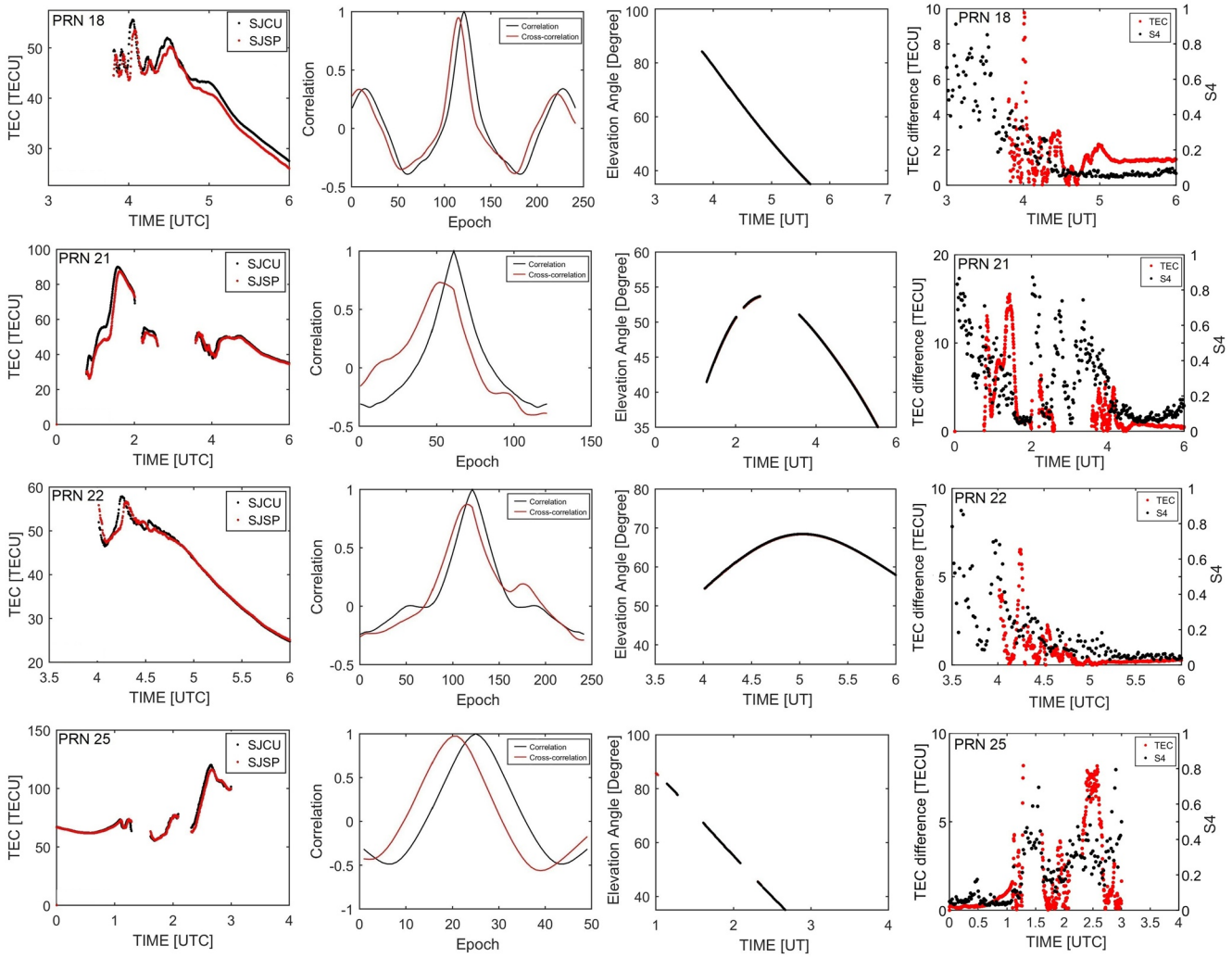

Figure 5. First column: time variation of the slant total electron content (TEC) values estimated at SJCU (black line) and SJSP (red line) reference stations; second column: cross-correlation between SJCU and SJSP slant TEC data (red line) and autocorrelation for SJCU reference station (black line); third column: elevation angle of the Global Positioning System (GPS) satellites; fourth column: comparation between TEC difference estimated for the reference stations (red dots) and S_4 data (black dots) for SJCU reference station. All plots were obtained for satellites PRN 18, 21, 22 and 25 (from top to bottom) on DOY 297.

occur in the late evening. It is not shown here but for this case on DOY 297 the ROTI varied between about 0.05–0.27, whose changes in TEC due to plasma bubbles can be classified from moderate to strong levels.

Similarly to Figure 5, but for the events of plasma bubbles that occurred on DOY 351 of 2014, the columns in Figure 6 present the results of slant TEC (1st column), autocorrelation and cross-correlation (2nd column), the elevation angles (3rd column), and the comparison between the TEC difference and S_4 values (4th column) of the GPS satellites PRN 04, 14, 19 and 27. For the satellites PRN 04 and 14 the measured TEC between around 04–06 UT presented signatures of depletions passing through short maxima and minima. The depletions attained maximum values of ~30 TECU and ~15 TECU for the satellites PRN 04 and 14 respectively; and occurred during the decrease in the TEC as the satellite elevation angle also decreased. Such decreases in TEC are related to the increase in the recombination process of the ionosphere during post-midnight hours. For the satellites PRN 19 and 27 the depletions in TEC were observed between around 02–04 UT. Although lack of TEC estimations was observed between around 02–03 UT for satellite PRN 19 due to loss of receiver lock associated with ionospheric scintillation presence, the plots suggest a depletion of ~25 TECU around this time. It is inspected from the plots that during the overpass of the satellites PRN 04 and 19 the depletions occurred when the TEC levels reduced from ~80 to 30 TECU. The ROTI (not shown

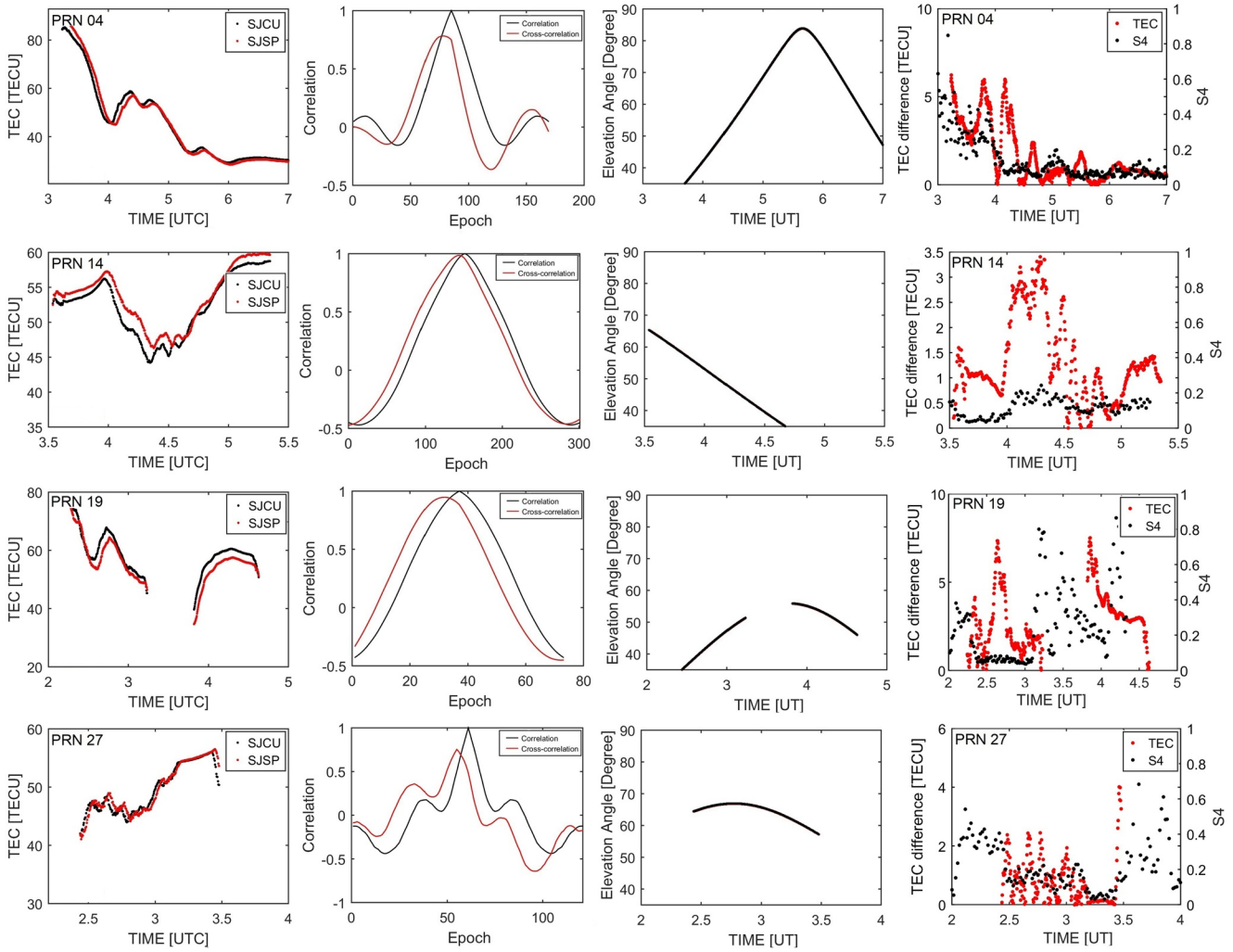

Figure 6. As in Figure 5 but for the case on DOY 351 and for satellites PRN 04, 14, 19 and 27 (from top to bottom).

here) attained values of ~0.25 near 02 UT, which also reveals for this case strong levels of changes in TEC associated to plasma bubbles.

In order to increase the number of velocity samples and to be able to estimate the mean velocity and standard deviation, the concept of sliding window was adopted in the estimation of plasma bubbles drift velocities. A sliding window of 18 min size with a time variation of 6 min was adopted.

Tables 1 and 2 summarize, respectively, for DOY 297 and 351 the time of TEC depletions registered for each GPS satellite, the mean and standard deviation zonal drift velocities obtained by sliding window during the observation of plasma bubble irregularities.

Table 1
Inferred Drift Velocities of the Equatorial Plasma Bubbles for the Case on DOY 297

PRN	Time [UTC]	Mean velocity [m/s]	Std deviation [m/s]
18	03:20	105.238	9.3476
21	04:00	66.111	13.356
22	04:30	105.778	34.624
25	01:09	136.000	-

It is inspected from Table 1 that for the case of DOY 297 the lowest drift velocity of 66.111 ± 13.356 m/s was inferred from TEC observations of the satellite PRN 21, whereas the highest velocity of 136 m/s was inferred from satellite PRN 25. It should be noted that it was not possible to estimate the mean and standard deviation zonal drift velocities form PRN 25 due to the short disturbed time period of fluctuating signals caused by the plasma bubble, that is the same size of the sliding window. Now considering the case that occurred on DOY 351, Table 2 shows that the

Table 2
Inferred Drift Velocities of the Equatorial Plasma Bubbles for the Case on DOY 351

PRN	Time [UTC]	Mean velocity [m/s]	Std deviation [m/s]
4	04:20	95.344	18.953
14	03:20	117.381	45.972
19	02:39	104.563	44.795
27	02:50	117.111	9.254

eastward drifts varied from 95.334 ± 18.953 to 117.381 ± 45.972 m/s. It is important to highlight that for some satellites they presented large standard deviation. This behavior can be explained due to the large delay between the TEC values on the two reference stations (SJSP and SJCU) caused by the presence of the plasma bubble, as can be seen in the first column in Figures 5 and 6. The epoch difference maximum autocorrelation and cross-correlation is associated with the EPBs traveling time. Therefore, the smaller difference between maximum autocorrelation and cross-correlation, smaller EPBs traveling time and greater EPBs zonal drift velocity. Furthermore, the epoch difference maximum autocorrelation and cross-correlation is influenced by too strong correlation between the reference stations due to the short distance between the GNSS stations. The same structure is recorded in both stations, that is, the EPBs cross one station after some time also cross the other.

The zonal drift velocities of the EPBs estimated in this present work were compared with the velocities inferred from all-sky imaging observations of the OI 630 nm nightglow emissions (Abalde et al., 2004; Pimenta et al., 2001). The all-sky linearized images were processed using the software Univap All-Sky Data Analysis (UASDA) developed by Pillat et al. (2009). From the linearized images the position and time of the airglow depletions are obtained, and the zonal velocities are estimated. The estimated zonal velocities were therefore limited to a range of 1,024 km centered over the imager zenith. Moreover, the deduced velocities refer to 300 km, the assumed height for the OI 630.0 nm airglow emitting layer.

The OI 630 nm emission images for the nights of October 24th, 2014 (DOY 297) and December 17th, 2014 (DOY 351) were recorded by the digital all-sky imager installed in the same site of the SJSP (23.21°S 45.86°W) GNSS reference station. Figures 7 and 8 show examples of a sequence of airglow images collected on the nights of DOY 297 and 351, respectively. The signatures of the plasma bubbles appear as dark bands across the images, which in fact are wavelike structures with near magnetic north-south aligned fronts (Sobral et al., 2009). The images were taken at 2-min cadence; however, the drift velocities were inferred for every four minutes of observation. It is clearly noted from the successive images presented in Figures 7 and 8 an eastward propagation of the plasma bubble depletions.

As previously mentioned, the all-sky imagers are dependent on weather conditions, where clouds and precipitation can disrupt the plasma bubbles imaging. In Figure 7, it is noted the degradation in image quality, probably due to the moisture or condensation on the camara over the night. Despite of the weather conditions, the plasma bubble depletion is evident on the airglow images.

The zonal drift velocities of the EPBs estimated in this present work were also compared with the velocities inferred from keograms technique, also based on all-sky OI 630-nm images (Vargas et al., 2020). The keograms were obtained from the cuts in all-sky linearized images considering different latitudes, for the DOYs 297 and 351. The Figures 9 and 10 show the keograms for different latitudes for DOY 297 and 351, respectively. In the keograms, the dark blue color represent depleted plasma density, that is, the signatures of the EPBs. The color scale in the keograms represents the level of depletion in plasma density. The zonal drift velocity can be calculated from the keograms by the relation between the zonal displacement (x-axis) and temporal variation (y-axis). In Figures 9 and 10 the plasma bubbles signatures are represented by dashed white line. Considering the different latitudes, it was possible to identify different ionospheric plasma bubble signatures. For DOY 297, maximum of 6 plasma bubbles were identified. For DOY 351, maximum of 8 plasma bubbles signatures were identified. Thus, from the different latitudes, it is possible to determine the mean velocity and standard deviation.

Figure 11 shows the temporal variation of the inferred zonal (eastward) velocities, deduced from the different methods. The measurement error bar plotted in black represents the mean velocities and standard deviation obtained by UASDA software using the successive OI 630 nm airglow images taken at 4-min intervals over São José dos Campos. The error bar plotted in blue is the mean velocities and standard deviation estimated by keogram technique, also using airglow images at São José dos Campos. In red, the mean plasma bubble velocities and the standard deviation calculated by the method proposed. The top panel of

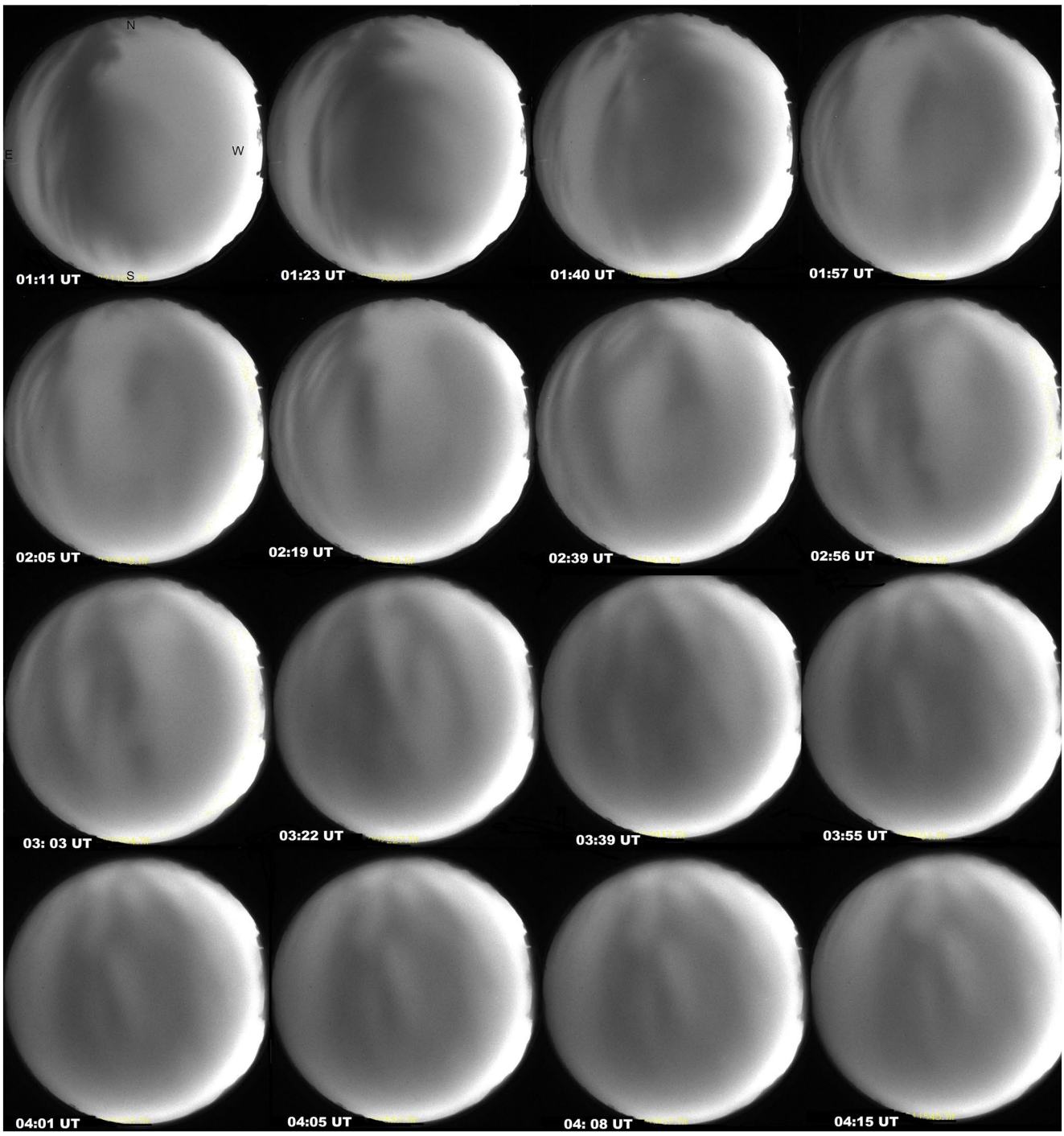

Figure 7. OI 630 nm airglow images at São José dos Campos for the time period between 01:11 and 04:15 UT on DOY 297, showing the eastward motion of the ionospheric plasma bubble depletions (the dark bands across the images).

Figure 11 shows the airglow velocities in the night of DOY 297, and the bottom panel the velocities inferred in the night of DOY 351. The mean ionospheric plasma bubble zonal drift was estimated by partial velocities that the UASDA software calculates. The partial velocities are estimated using linearized images where horizontal cuts are made by selecting a column from a matrix of 512 × 512. The analysis of cuts in the consecutive image allows us to obtain the displacement in time of the profile which represents the velocity of the structure in observed space. The zonal drift velocities were inferred with different intervals, for the OI

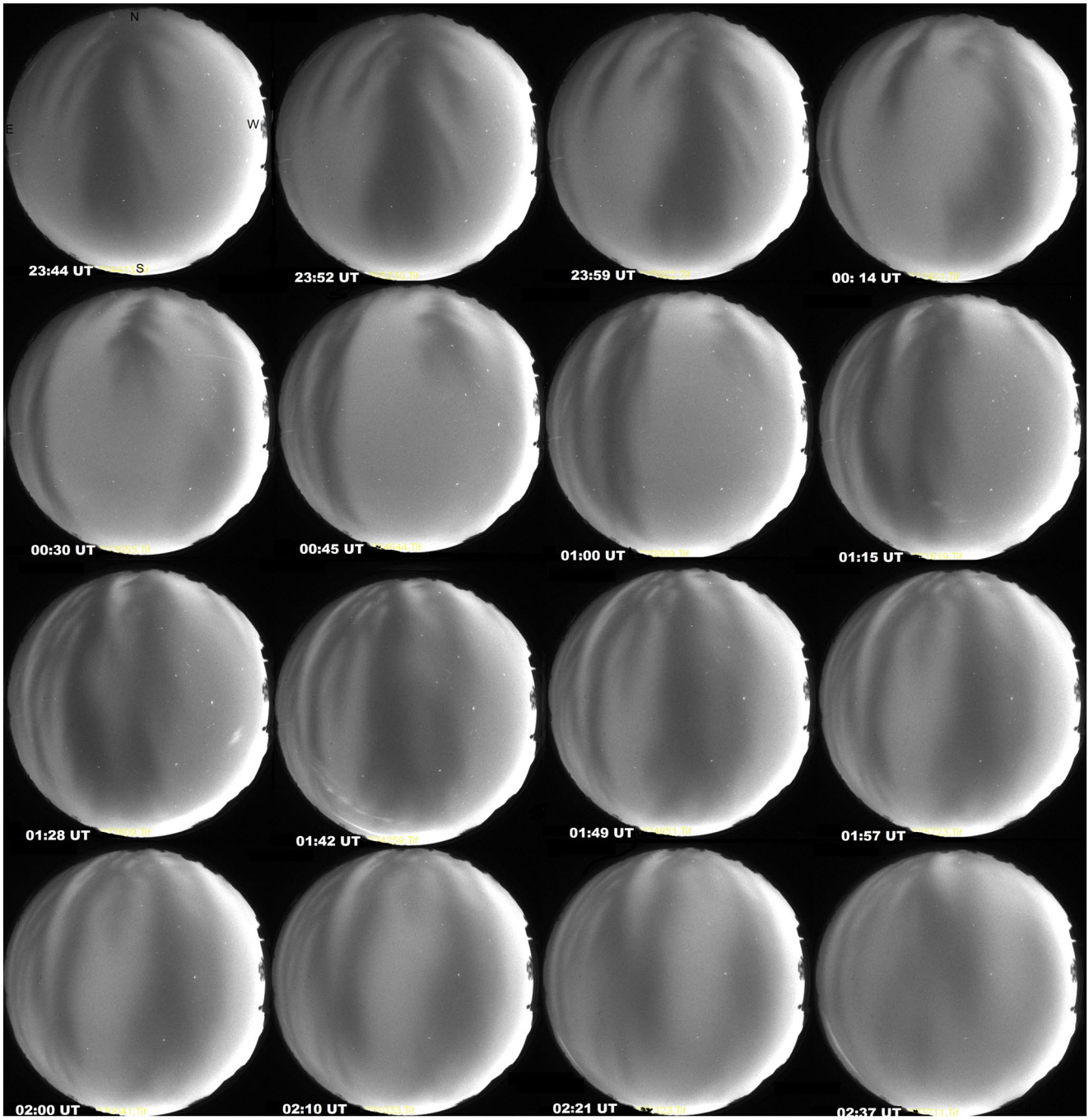

Figure 8. OI 630 nm airglow images at São José dos Campos for the time period between 23:44 and 02:37 UT on DOY 351, showing the eastward motion of the ionospheric plasma bubble depletions (the dark bands across the images).

630 nm airglow all-sky images process, mainly due to the limitations of the software when selecting the EPB small internal structures and bifurcations, besides the difficult detection of the bubbles on the edges of the images. The mean and standard deviation velocities estimated by the method proposed were calculated by sliding windown during the interval time of the plasma bubbles occurrence. The velocities were estimated every 18 min with temporal resolution of 6 min.

Considering the zonal velocities obtained by UASDA software, in top panel of Figure 11 we note that the zonal velocities in the night of DOY 297 was ~138 m/s around 03 UT. Then the zonal velocities were

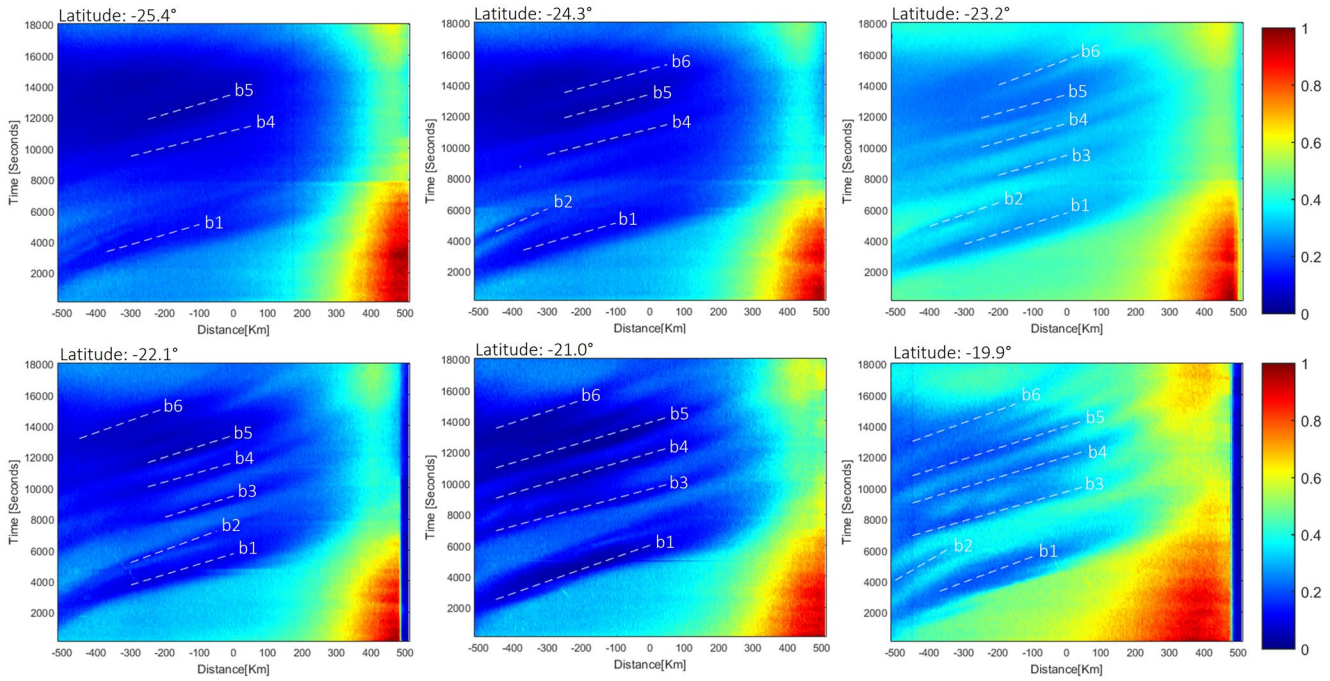

Figure 9. Keograms based on airglow images at São José dos Campos on DOY 297, considering different latitudes. The regions of equatorial plasma bubbles (EPBs) are represented by blue dark color in keograms. The dashed white line represents an interval that is possible to infer the plasma bubbles velocities.

followed by a decrease and reached ~60 m/s around 04:30 UT. This decrease of the eastward drift velocity with time agrees with previous observations at low latitudes (Abalde et al., 2004; Muella et al., 2017). As can be seen for bottom of Figure 11, in the night of DOY 351 the magnitude of the zonal velocities were ~110 m/s at 00:15 UT, which was followed by a decrease until around 00:50 UT, and then rapidly increased

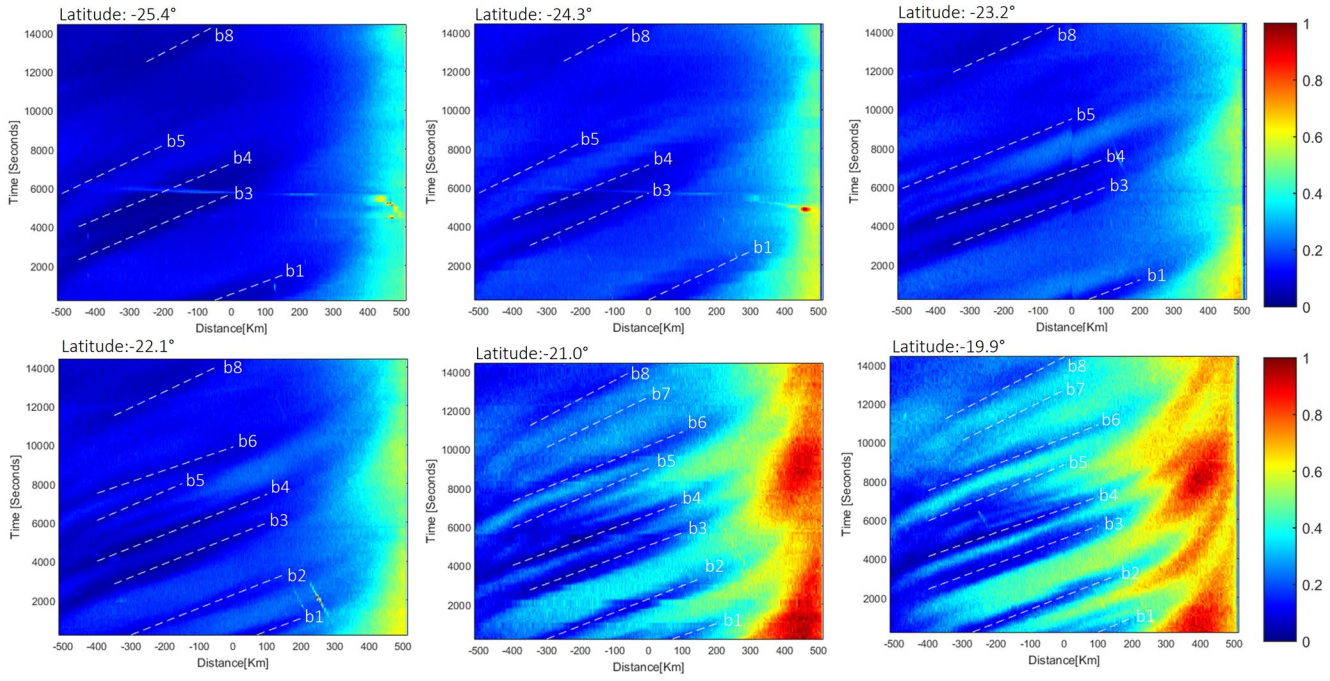

Figure 10. Keograms based on airglow images at São José dos Campos on DOY 351, considering different latitudes. The regions of equatorial plasma bubbles (EPBs) are represented by blue dark color in keograms. The dashed white line represents an interval that is possible to infer the plasma bubbles velocities.

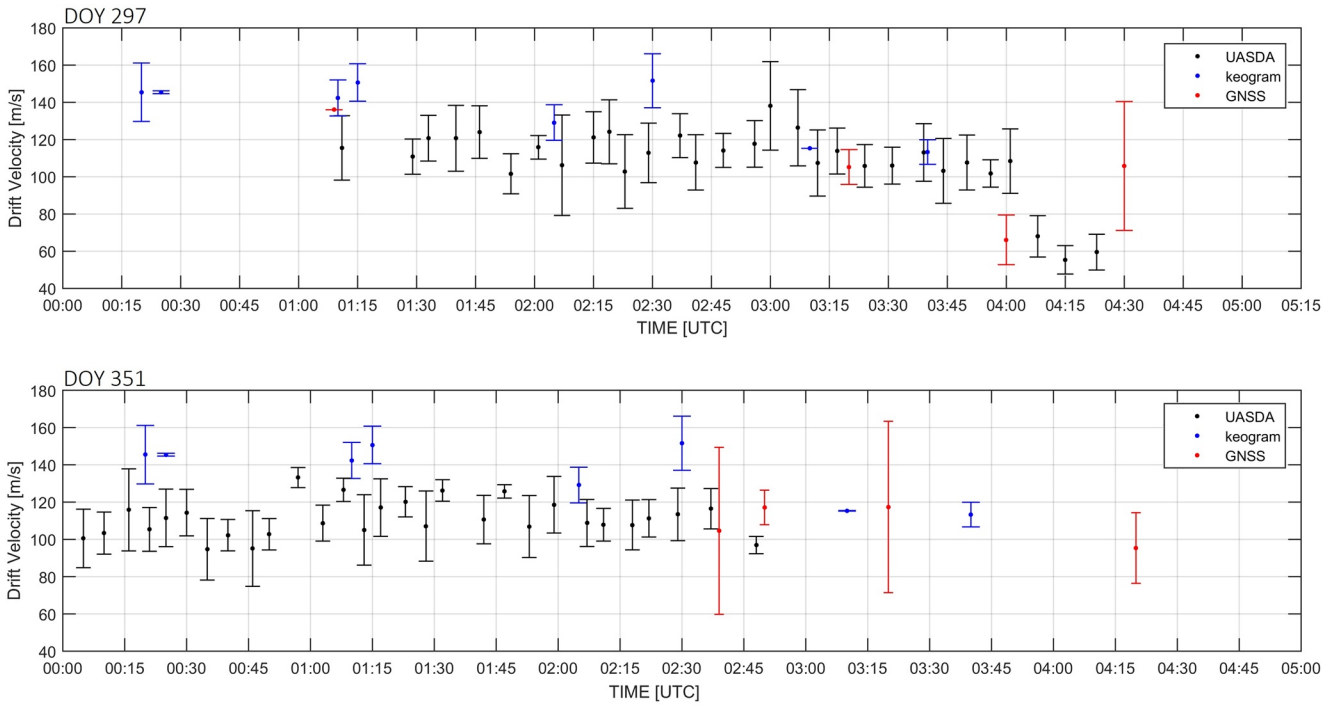

Figure 11. Temporal variation (in universal time) of the nighttime airglow velocities over São José dos Campos on DOY 297 (top panel) and DOY 351 (bottom panel) of 2014. The vertical bars denote standard deviation. The black color represents the velocities obtained by UASDA software. The blue color are the velocities obtained by keograms. The red color represents the similar velocities obtained by the method proposed.

to a maximum of ~133 m/s around 01 UT. Then the magnitude of the zonal drift velocities decreased with some brief reversals until its minimum value of ~97 m/s around 02:50 UT. The same behavior can be observed with the velocities obtained from keogram. In both nights, until 03:00 UT the magnitude of the zonal velocities were ~140 m/s which was followed by a decrease with zonal velocities of ~120 m/s.

Despite of the small time overlap between the all-sky velocities and the proposed method, the results were comparable. The mean ionospheric plasma bubble zonal drift over São José dos Campos inferred from all-sky imaging, using UASDA software, during the night of DOY 297 was 104.219 ± 21.921 m/s. This result is in fairly good agreement with the mean zonal drifts of 103.282 ± 28.648 m/s derived from TEC measurements over the reference stations of SJCU and SJSP. Considering the keogram technique the mean zonal drifts is 141.217 ± 20.605 m/s. For the night of DOY 351 our results are also in accordance with those observed from GNSS observations at São José dos Campos. From the TEC calculations the mean zonal drift velocities on DOY 351 was 108.600 ± 10.670 m/s, whereas from the optical techniques the values of mean velocities were 111.1869 ± 9.148 m/s (UASDA) and 136.644 ± 15.417 m/s (keograms).

As noted, the mean zonal drifts deduced from GPS TEC present larger vertical variance bars when compared with the results from the optical technique. As the GPS satellites move, their signals puncture the plasma bubbles at different elevation angles and locations in the sky, hence the GPS-estimated zonal drifts tend to be more spread in velocity. Otherwise, the plasma bubble drifts from OI 630.0 nm all-sky imaging were deduced from a narrower altitude range around 300 km.

The bubble drift velocities estimated in this work were comparable with those reported in previous studies. Takahashi et al. (2015) estimated the plasma bubbles velocities using two methods: keogram and TECMAP. The keogram method is based on east–west slices cutting the all-sky images passing over the local zenith and plotted as a function of time. The TECMAP method is based on TEC data mapped on the ionospheric shell at 300 km. In their study the velocities were estimated for the CHPI station (22,7°S, 45,0°W), located in Cachoeira Paulista/SP, on the night of December 24–25, 2013. For example, from the horizontal gradient of the zonal component in the keogram, the longitudinal drift velocity estimated was 159 ± 10 m/s, whereas from the TECMAP the zonal drift velocity was 153 ± 15 m/s. Haase et al. (2010) also estimated

the bubble drift velocities by using two methods, that is airglow data and GPS vertical TEC data. In their work, the propagation velocity from TEC was estimated by the time of occurrence of plasma depletion seen at different GPS stations within the 30 s time resolution of the data samples. A time series with the airglow images was constructed to estimate the plasma bubble velocities. The airglow velocities were calculated for Fazenda Santa Isabel (47.60°S, −14.67°W), Brazil, from September to November 2005. The authors showed that the irregularities from both techniques drifted at velocities ranging from ∼85 to 110 m/s, reducing their magnitude as the night progressed. Ji et al. (2011) estimated the ionospheric zonal drifts by using GPS references stations. In their study, the zonal drift velocities at 350 km were estimated based on the diffraction pattern delay between ground receivers and using the cross-correlation technique. The velocities were estimated for two different areas: California (midlatitude) and Hong Kong (low latitude). The velocities estimated for the middle latitude station were higher (∼100–200 m/s) when compared to previous studies, whereas for the low latitude station the velocities assumed values of 100–200 m/s in the evening hours and after midnight decreased over the time. More recently, Silva et al. (2019) also estimated plasma bubble zonal drift from TEC data. A methodology of pattern recognition was developed and implemented using the Long-Term Ionospheric Anomaly Monitoring (LTIAM), by using two GNSS stations close to each other and compared the results with velocities obtained calculated by keogram technique based on all-sky images. The velocities were estimated at SSA1(12.97°S, 38.52°W) and SAVO stations (12.94°S, 38.43°W), Brazil, for the years of 2012, 2013 and 2014, considering 10 representative days of the months from September to January. In their study, the higher velocities (∼300 m/s) were observed during the evening, and then abated to ∼60 m/s in the later hours of the night. The authors concluded that there were no significant differences between the speeds calculated by the LTIAM technique and keogram. In general, the velocities estimated in this present work are in agreement with those reported from the previous studies, with magnitudes ranging between around ∼70–140 m/s.

5. Summary and Conclusions

In this study, the zonal drift velocities of the EPBs were inferred from slant TEC estimations from pairs of GNSS reference stations located at low latitudes. We analyzed the velocities obtained for different data sampling, and we observed that for the lower sampling rate (15 s) the drift velocities seems to be more accurate than the velocities obtained by larger sampling rates (30 s). Therefore, the TEC values were calculated from 1/15s sampling rate of GNSS data. We used the cross-correlation and autocorrelation techniques to estimate the traveling time of the plasma bubbles between the two stations. The bubble drifts were deduced at sites located near the international airports of RJ and São José dos Campos. Three cases of plasma bubble observations during months of large occurrence of ionospheric irregularities were considered in the analysis. One case that occurred in January of 2014 was analyzed at the reference stations of RJ, and other two cases (October and December 2014) were analyzed at the reference stations of São José dos Campos. The results obtained over São José dos Campos were compared with the drift velocities estimated from nighttime airglow techniques such as UASDA and keograms.

Depending on the satellite elevation angle, the TEC-estimated plasma bubbles drifted eastward with velocities ranging ∼70–140 m/s in 00–05 UT (21–02 LT). As expected, the velocities presented some temporal variability, with their magnitudes decreasing after local midnight hours owing to the natural decay of the plasma bubble irregularities. Simultaneous observations of ionospheric irregularities from all-sky imaging system revealed large-scale plasma bubble structures over São José dos Campos coexisting with the TEC depletions. The nighttime airglow images also revealed the eastward movement of the plasma bubbles. Considering the airglow techniques UASDA and keogram, in the evening hours the airglow velocities increased not monotonically until their maximum of ∼130–140 m/s between around 01–03 UT, and then it decreased to ∼60 m/s after midnight. Despite of the small time overlap between the methods presented here, the estimated velocities are in good agreement, since the results were fully compliant with the airglow technique. For the two cases analyzed,the results showed that the mean zonal drift velocities derived from the GPS slant TEC calculations are comparable with the mean velocities estimated from the airglow techniques.

Compared with other observations in the Brazilian low-latitude region, the results from our technique are also in agreement to the values of zonal drift velocities published in the literature. In that sense, future studies of drift velocities are expected to include the others GNSS constellations, such as Galileo, GLONASS

and Beidou, with simultaneous measurements at different latitude and longitude sectors. In addition, we can also investigate the influence of the seasonal, solar cycle and geomagnetic storms on the variability of plasma bubbles drift velocities. For GBAS to be implemented in equatorial regions, such as Brazil case, more studies of the characteristics of gradients associated with plasma bubbles are necessary. Besides propagation velocities, more studies on spatial scale sizes, orientations are needed.

Data Availability Statement

The authors acknowledge the RBMC network for making data available (https://www.ibge.gov.br/geociencias/downloads-geociencias.html).

Acknowledgments
A. L. C. Souza acknowledges the support from Conselho Nacional de Desenvolvimento Cientifico e Tecnológico (CNPq) and also INCT GNSS-NavAer supported by CNPq (465648/2014-2), CAPES (23038.000776/2017-54) e FAPESP (2017/50115-0). P. O. Camargo thanks CNPq (479965/2013-7 and 309924/2013-8). M. T. A. Muella thanks CNPq for the support under grant 310829/2017-8. The authors are grateful to Valdir Pillat for providing the UASDA software.

References

Abalde, J. R., Fagundes, P. R., Sahai, Y., Pillat, V. G., Pimenta, A. A., & Bittencourt, J. A. (2004). Height-resolved ionospheric drifts at low latitudes from simultaneous OI 777.4 nm and OI 630.0 nm imaging observations. *Journal of Geophysical Research*, *109*, A11308. https://doi.org/10.1029/2004JA010560

Abdu, M. A. (2005). Equatorial ionosphere–thermosphere system: Electrodynamics and irregularities. *Advances in Space Research*, *35*(5), 771–787. https://doi.org/10.1016/j.asr.2005.03.150

Brassarote, G. D. O. N., de Souza, E. M., & Monico, J. F. G. (2018). S 4 index: Does it only measure ionospheric scintillation? *GPS Solutions*, *22*(1), 1–12. https://doi.org/10.1007/s10291-017-0666-x

Bumrungkit, A., Rungraengwajiake, S., Supnithi, P., & Siansawasdi, N. (2014). Drift velocity estimation of ionospheric disturbance using GPS observations. In *The 4th Joint International Conference on Information and Communication Technology, Electronic and Electrical Engineering (JICTEE)*. IEEE (pp. 1–5). https://doi.org/10.1109/JICTEE.2014.6804061

Bumrungkit, A., Supnithi, P., & Saito, S. (2018). Statistical Analysis of Separation Distance Between Equatorial Plasma Bubbles Near Suvarnabhumi International Airport, Thailand. *Journal of Geophysical Research: Space Physics*, *123*(9), 7858–7870. https://doi.org/10.1029/2018JA025612

Ciraolo, L., Azpilicueta, F., Brunini, C., Meza, A., & Radicella, S. M. (2007). Calibration errors on experimental slant total electron content (TEC) determined with GPS. *Journal of Geodesy*, *81*(2), 111–120. https://doi.org/10.1007/s00190-006-0093-1

Fujiwara, T., & Tsujii, T. (2016). GBAS availability assessment and modeling of ionospheric scintillation effects. *Navigation: Journal of the Institute of Navigation*, *63*(4), 405–413. https://doi.org/10.1002/navi.160

Haase, J. S., Dautermann, T., Taylor, M. J., Chapagain, N., Calais, E., & Pautet, D. (2010). Propagation of plasma bubbles observed in Brazil from GPS and airglow data. *Advances in Space Research*, *47*(10), 1758–1776. https://doi.org/10.1016/j.asr.2010.09.025

Ji, S., Chen, W., Ding, X., & Zhao, C. (2011). Equatorial ionospheric zonal drift by monitoring local GPS reference networks. *Journal of Geophysical Research*, *116*, A08310. https://doi.org/10.1029/2010JA015993

Kelley, M. C. (2009). *The Earth's ionosphere: Plasma physics and electrodynamics*. Academic press.

Mannucci, A. J., Wilson, B. D., Yuan, D. N., Ho, C. H., Lindqwister, U. J., & Runge, T. F. (1998). A global mapping technique for GPS-derived ionospheric total electron content measurements. *Radio Science*, *33*(3), 565–582. https://doi.org/10.1029/97RS02707

Mendillo, M., Zesta, E., Shodhan, S., Sultan, P. J., Doe, R., Sahai, Y., & Baumgardner, J. (2005). Observations and modeling of the coupled latitude-altitude patterns of equatorial plasma depletions. *Journal of Geophysical Research*, *110*, A09303. https://doi.org/10.1029/2005JA011157

Muella, M. T. A. H., Duarte-Silva, M. H., Moraes, A. O., de Paula, E. R., de Rezende, L. F. C., Alfonsi, L., & Affonso, B. J. (2017). Climatology and modeling of ionospheric scintillations and irregularity zonal drifts at the equatorial anomaly crest region. *Annales Geophysicae*, *35*(6), 1201–1218. https://doi.org/10.5194/angeo-35-1201-2017

Pereira, V. A. S., & Camargo, P. O. (2017). Brazilian active GNSS networks as systems for monitoring the ionosphere. *GPS Solutions*, *21*(3), 1013–1025. https://doi.org/10.1007/s10291-016-0589-y

Pi, X., Mannucci, A. J., Lindqwister, U. J., & Ho, C. M. (1997). Monitoring of global ionospheric irregularities using the worldwide GPS network. *Geophysical Research Letters*, *24*(18), 2283–2286. https://doi.org/10.1029/97gl02273

Pillat, V. G., Guedes, J. R. A., & Fagundes, P. R. (2009). Programa para análise de imagens dos fotômetros imageadores UASDA- Univap All Sky Data Analysis. In *Anais XIV Simpósio Brasileiro de Sensoriamento Remoto* (pp. 1691–1698).

Pimenta, A. A., Fagundes, P. R., Bittencourt, J. A., Sahai, Y., Gobbi, D., Medeiros, A. F. D., et al. (2001). Ionospheric plasma bubble zonal drift: A methodology using OI 630 nm all-sky imaging systems. *Advances in Space Research*, *27*(6–7), 1219–1224. https://doi.org/10.1016/S0273-1177(01)00201-0

Prol, F. S., Camargo, P. O., Monico, J. F. G., & Muella, M. T. A. H. (2018). Assessment of a TEC calibration procedure by single-frequency PPP. *GPS Solutions*, *22*(2). https://doi.org/10.1007/s10291-018-0701-6

Prol, F. S., Hernández-Pajares, M., Muella, M. T. A. H., & Camargo, P. O. (2018). Tomographic imaging of ionospheric plasma bubbles based on GNSS and radio occultation measurements. *Remote Sensing*, *10*(10), 1529. https://doi.org/10.3390/rs10101529

Rungraengwajiake, S., Supnithi, P., Saito, S., Siansawasdi, N., & Saekow, A. (2015). Ionospheric delay gradient monitoring for GBAS by GPS stations near Suvarnabhumi airport, Thailand. *Radio Science*, *50*(10), 1076–1085. https://doi.org/10.1002/2015RS005738

Sahai, Y., Fagundes, P. R., Bittencourt, J. A. (2000). Transequatorial F-region ionospheric plasma bubbles: solar cycle effects. *Journal of Atmospheric and Solar-Terrestrial Physics*, *62*(15), 1377–1383.

Saito, S., Sunda, S., Lee, J., Pullen, S., Supriadi, S., Yoshihara, T., et al. (2017). Ionospheric delay gradient model for GBAS in the Asia-Pacific region. *GPS Solutions*, *21*(4), 1937–1947. https://doi.org/10.1007/s10291-017-0662-1

Silva, R. P., Souza, J. R., Sobral, J. H. A., Denardini, C. M., Borba, G. L., & Santos, M. A. F. (2019). Ionospheric plasma bubble zonal drift derived from total electron content measurements. *Radio Science*, *54*(7), 580–589. https://doi.org/10.1029/2018RS006727

Sobral, J. H. A., Abdu, M. A., Pedersen, T. R., Castilho, V. M., Arruda, D. C. S., Muella, M. T. A. H., et al. (2009). Ionospheric zonal velocities at conjugate points over Brazil during the COPEX campaign: Experimental observations and theoretical validations. *Journal of Geophysical Research*, *114*, A04309. https://doi.org/10.1029/2008ja013896

Srinivas, V. S., Sarma, A. D., Reddy, A. S., & Reddy, D. K. (2014). Investigation of the effect of ionospheric gradients on GPS signals in the context of LAAS. *Progress in Electromagnetics Research*, *57*, 191–205. https://doi.org/10.2528/PIERB13101305

Stefanello, M. B., Muella, M. T. A. H., Amorim, D. C. M., Machado, C. S., Bageston, J. V., Pimenta, A. A., et al. (2015). OI 630.0 nm all-sky image observations of medium-scale traveling ionospheric disturbances at geomagnetic conjugate points. *Journal of Atmospheric and Solar-Terrestrial Physics*, *128*, 58–69. https://doi.org/10.1016/j.jastp.2015.03.012

Takahashi, H., Wrasse, C. M., Otsuka, Y., Ivo, A., Gomes, V., Paulino, I., et al. (2015). Plasma bubble monitoring by TEC map and 630 nm airglow image. *Journal of Atmospheric and Solar-Terrestrial Physics*, *130–131*, 151–158. https://doi.org/10.1016/j.jastp.2015.06.003

Vani, B. C., Shimabukuro, M. H., Galera Monico, J. F. (2017). Visual exploration and analysis of ionospheric scintillation monitoring data: The ISMR Query Tool. *Computers & Geosciences*, *104*, 125–134. https://doi.org/10.1016/j.cageo.2016.08.022

Vargas, F., Brum, C., Terra, P., & Gobbi, D. (2020). Mean zonal drift velocities of plasma bubbles estimated from keograms of nightglow all-sky images from the Brazilian sector. *Atmosphere*, *11*(1), 69. https://doi.org/10.3390/atmos11010069

Wang, G. J., Shi, J. K., Reinisch, B. W., Wang, X., & Wang, Z. (2015). Ionospheric plasma bubbles observed concurrently by multi-instruments over low-latitude station Hainan. *Journal of Geophysical Research: Space Physics*, *120*, 2288–2298. https://doi.org/10.1002/2014ja020245

Yang, Z., & Liu, Z. (2018). Low-latitude ionospheric density irregularities and associated scintillations investigated by combining COSMIC RO and ground-based global positioning system observations over a solar active period. *Journal of Geophysical Research: Space Physics*, *123*, 3998–4014. https://doi.org/10.1029/2017JA024199

Yoon, M., Kim, D., Pullen, S., & Lee, J. (2019). Assessment and mitigation of equatorial plasma bubble impacts on category I GBAS operations in the Brazilian region. *Navigation*, *66*(3), 643–659. https://doi.org/10.1002/navi.328